Chemical
Science

ROYAL SOCIETY
OF CHEMISTRY

EDGE ARTICLE

View Article Online
View Journal | View Issue

Check for updates

Cite this: *Chem. Sci.*, 2023, **14**, 1320

All publication charges for this article have been paid for by the Royal Society of Chemistry

Received 4th November 2022
Accepted 9th January 2023

DOI: 10.1039/d2sc06085j

rsc.li/chemical-science

Conductivity and photoconductivity in a two-dimensional zinc bis(triarylamine) coordination polymer†

Chin May Ngue, *[a] Kuan Fu Ho,[b] Batjargal Sainbileg,[d] Erdembayalag Batsaikhan,[d] Michitoshi Hayashi,[d] Kuei Yi Lee,[b] Ruei San Chen *[c] and Man Kit Leung *[a]

We report the synthesis and characterization of a 2D semiconductive and photoconductive coordination polymer. [Zn(TPPB)(Cl$_2$)]·H$_2$O (**1**) (TPPB = N^1,N^1,N^4,N^4-tetrakis(4-(pyridin-4-yl)phenyl)benzene-1,4-diamine) consists of a TPPB redox-active linker with bis(triarylamine) as the core. It consists of two redox sites connected with a benzene ring as a bridge. Thus, this forms an extended conjugation pathway when the TPPB ligand is coordinated with the Zn^{2+} metal ions. The single crystal conductivity measurement revealed conductivity of **1** to be in the range of 0.83 to 1.9 S cm^{-1}. Band structure analysis predicted that **1** is a semiconductor from the delocalization of electronic transport in the network. The computational calculations show the difference in charge distribution between holes and electrons, which led to spatial separation. This implies a long charge carrier lifetime as indicated by lifetime measurement. Incorporating a bis(triarylamine)-based redox-active linker could lead to a new semiconductive scaffold material with photocatalytic applications.

Introduction

2D coordination polymers (C. P.) are one of the emerging layered materials that offer unprecedented structure diversity and physical properties. They exhibit in-plane charge delocalization and efficient π-conjugation, resulting in high charge carrier mobility.[1] Despite the non-porous nature of 2D C. P., by judicious selection of organic linkers and transition metal ions, these materials potentially offer distinctive electronic properties.[2–4]

A few examples of conductive 2D C. P. with a single crystal structure exist.[5–7] Most are obtained as crystalline powders.[2,3,8–11] The lack of single crystal structures has restrained our knowledge of structure–property relationships with atomic precision.[12–14] Powder X-ray diffraction and quantum calculations are used to predict the structure of 2D C. P.; the combined approach offers limited structural information. It provides vague insights into atomic positions, stacking layers, and geometric parameters.[12] In this paper, we successfully obtained single crystal structure data that precisely describe the packing and bonding.

The incorporation of redox-active linkers, like dithiolenes,[1,3,9,15–21] semiquinones/cathecolates,[22–29] diimines,[30] and naphthalenetetracarboxydiimide[31] into the network has resulted in the network possessing intriguing electronic properties. Another family of redox-active linkers, which is triarylamine, has received little attention. In view of this, a new redox-active linker with an electron-donating nature, a bis(triarylamine) derivative was designed - N^1,N^1,N^4,N^4-tetrakis(4-(pyridin-4-yl)phenyl)benzene-1,4-diamine (TPPB), and incorporated with the metal ion, Zn^{2+} (Fig. 1a). Triarylamine is well-known for its electron-donating nature and has been used widely as a hole transport molecule in optoelectronic materials.[32,33] The TPPB ligand consists of two redox centers bridged with a benzene ring with *para* substitution. This forms an extended π-conjugated pathway. The current application of the TPPB ligand in the coordination framework mainly describes the variation of the crystal structure.[34]

By incorporating a redox-active TPPB linker with conjugated organic moieties into the network, we envisage that electron transfer and transport dominate the assembled network. This further urges us to investigate the photocurrent properties of a coordination polymer. By definition, the current is monitored as a function of the applied voltage for a conjugated 2D network

---

[a] *Department of Chemistry, National Taiwan University, Taipei 106, Taiwan. E-mail: chinmayngue@ntu.edu.tw; mkleung@ntu.edu.tw*

[b] *Graduate Institute of Electro-Optical Engineering, National Taiwan University of Science and Technology, Taipei 106, Taiwan*

[c] *Graduate Institute of Applied Science and Technology, National Taiwan University of Science and Technology, Taipei 106, Taiwan. E-mail: rsc@mail.ntust.edu.tw*

[d] *Center for Condensed Matter Sciences, Center of Atomic Initiative for New Materials, National Taiwan University, Taipei 106, Taiwan*

† Electronic supplementary information (ESI) available: Synthesis of materials, physical characterization, conductivity and photoconductivity measurements, and computational details. CCDC 2173865. For ESI and crystallographic data in CIF or other electronic format see DOI: https://doi.org/10.1039/d2sc06085j

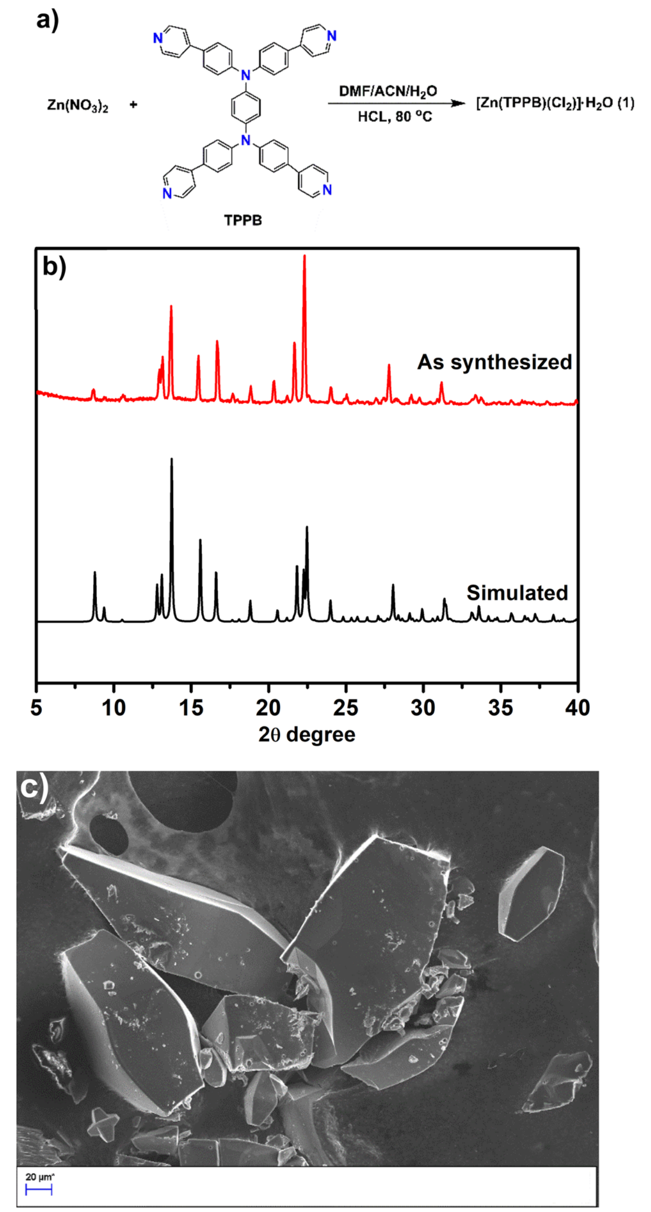

Fig. 1 (a) The synthetic scheme, (b) powder X-ray diffraction patterns of simulated and as-synthesized **1**, and (c) scanning electron microscopy (SEM) image of **1**.

between two leads.[35] The applied voltage modulated the electronic states.

Herein, incorporating the TPPB linker with Zn^{2+} metal ions afforded a 2D coordination polymer. The electrochemical analysis observed electronic communication between two redox-active sites with two reversible oxidation waves. Scan rate-dependent analysis verified that the dominant mechanism is charge-hopping. Two-probe single-crystal conductivity measurements revealed conductivity to be in the range of 0.83 to 1.90 S cm^{-1}. Band structure analysis confirms that the semiconductive behavior arises from the strong delocalization of electrons between the triarylamine linkers. The photocurrent displayed a linear relationship between the current and optical intensity. As predicted by the valence band maximum (VBM) and conduction band minimum (CBM), a spatial charge distribution caused by holes and electrons resulted in slow charge recombination and a long carrier lifetime.

Results and discussion

Our molecular design for producing a semiconductive and photoconductivity crystal structure came directly from a bottom-up self-assembly process: the self-assembly process between TPPB ligands embedded with a first-row transition metal, Zn^{2+} (Fig. 1a). We focused on N^1,N^1,N^4,N^4-tetrakis(4-(pyridin-4-yl)phenyl)benzene-1,4-diamine (TPPB) as a redox-active organic linker. This molecular design was inspired by the good π-conjugation and electron donor abilities of bis(triarylamine). For the TPPB linker, two redox centers are connected through a bridging benzene ring with *para*-substitution. The key concepts of *para*-conjugation have been adopted in organic chemistry to design conjugated materials; it helps to tune effective electronic communication in an extended π-conjugated system.[36] The electronic communication between two redox sites can be observed in the electrochemical experiment. It gave rise to two reversible oxidation waves.[37] The strategy of direct integration of the TPPB ligand with Zn^{2+} metal ions afforded a two-dimensional network. To date, several coordination polymers have been reported using the same organic core as the linker;[34,38] however, charge transport behavior in the 2D coordination polymer has remained unexplored.

The single crystal of **1** was obtained by reacting the TPPB linker, $Zn(NO_3)_2$, DMF, water, concentrated hydrochloric acid, and acetonitrile at 80 °C (Fig. 1a). Powder X-ray diffraction (PXRD) (Fig. 1b) confirmed the integrity and crystallinity of **1**. An orange prism single crystal (Fig. 1c and S5†) was obtained, $[Zn(TPPB)(Cl_2)]\cdot H_2O$ (**1**). Single crystal X-ray diffraction analysis revealed that **1** crystallized in the orthorhombic phase with a *Ccca* space group. Each Zn^{2+} metal ion is coordinated with two nitrogens from the pyridine and two chloride ions (Fig. 2a).

Coordination of Zn^{2+} metal ions with the TPPB linker resulted in hexagonal channels when viewed under a single network (Fig. 2b and d). A continuous π-conjugated backbone allows efficient charge transport based on this single network. **1** is a densely interpenetrating framework, as illustrated in Fig. 2c; it forms a non-porous coordination polymer. The Brunauer–Emmett–Teller (BET) surface area by N_2 adsorption analysis at 77 K confirmed the non-porous nature of **1**. The BET surface area is 12.83 $m^2\ g^{-1}$ (Fig. S7†). Furthermore, PLATON[39] calculation gave a void accessible of 12. 1%. We performed the thermal gravimetric analysis (TGA) to investigate the thermal stability of **1**. As shown in Fig. S4b,† the initial weight loss indicates the liberation of water. After 530 °C, **1** decomposed gradually.

Redox chemistry

It is well-established that incorporating redox-active linkers into coordination frameworks resulted in an electron hopping mechanism within a regular array of fixed sites,[40,41] as evidenced

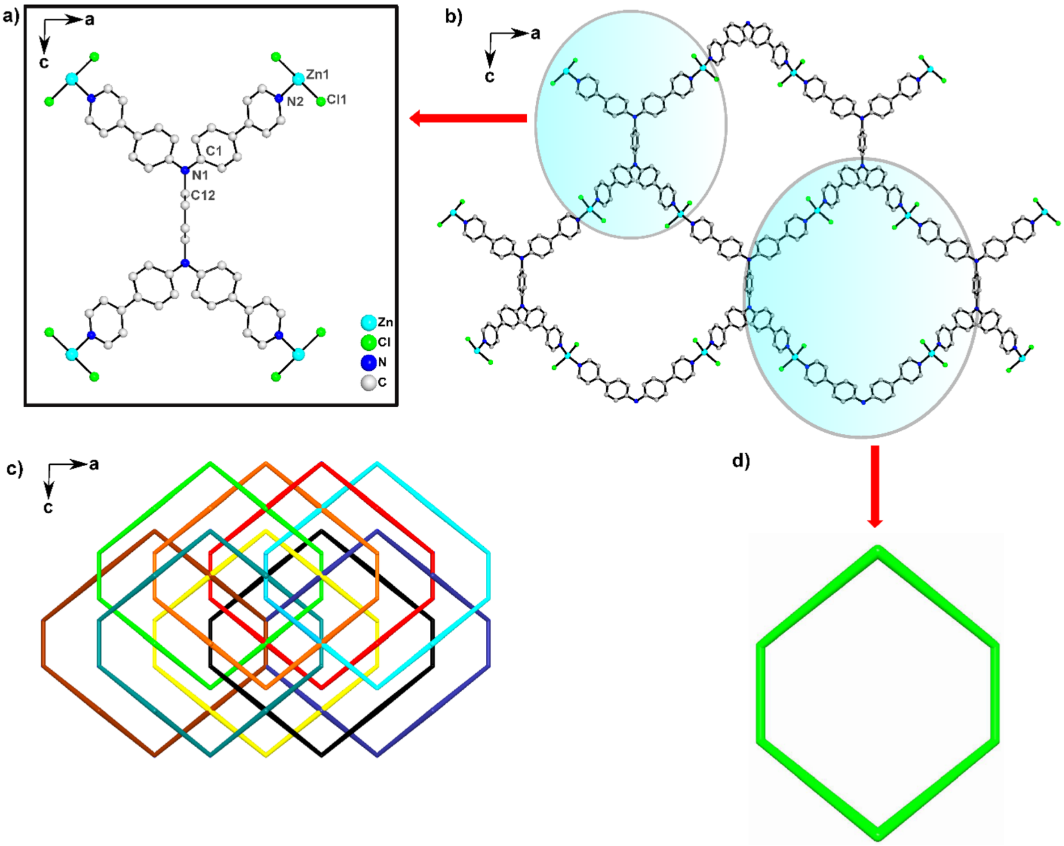

Fig. 2 (a) Coordination environments of **1**, (b) a single network, (c) a dense interpenetrating framework, and (d) topology of a hexagonal channel.

by the electrochemical methods. Charge transport in the framework can be considered as the diffusion of electrons.[42] The incorporation of a redox-active TPPB linker into the Zn-framework allowed us to investigate the electrochemical behavior of **1** by cyclic voltammetry.

Solid-state cyclic voltammetry (CV) analysis of **1** (Fig. 3) in 0.1 M n-Bu_4NPF_6/CH_2Cl_2 shows two reversible waves between 0.28 V and 0.7 *vs.* Fc/Fc^+ from consecutive one-electron oxidation of each of the two triarylamine redox sites (Fig. 3). The obtained values matched well with those recorded for the TPPB linker (Fig. S8†). The results confirmed that the electron-donating nature of the triarylamine-based units was retained in **1**. Theoretically, an ideal case of a fully reversible wave will have a peak separation of 59 mV/n at 25 °C, where n is the number of electrons involved. Due to uncompensated ohmic drops in the electrochemical setup (*vide infra*), it is impossible to observe the peak separation magnitude. In the conventional experiment, reversibility is defined at approximately 120 mV/n.[40] Based on this assumption, the first two electrochemical waves in **1** are reversible. For the first and second oxidation, we observed a nonzero peak separation of $E_p = 90$ mV at both waves.

Upon changing the scan rate from 25 mV s^{-1} to 100 mV s^{-1}, a statistically linear relationship curve fitted between the peak current i_{pc} and the square root of the scan rate $(V\ s^{-1})^{1/2}$ for the first ($r^2 = 0.99$, inset of Fig. 3) and second oxidation ($r^2 = 0.97$, inset of Fig. 3).[43] From the plot of the second oxidation wave i_{pc} *vs.* $(V\ s^{-1})^{1/2}$, a curvature was observed. Both the current responses obey the Randles–Sevcik equation.[40] The electron transfer process in **1** is followed by a diffusion-limited effect *via* electron hopping between the TPPB linkers and counterions from the electrolytes.

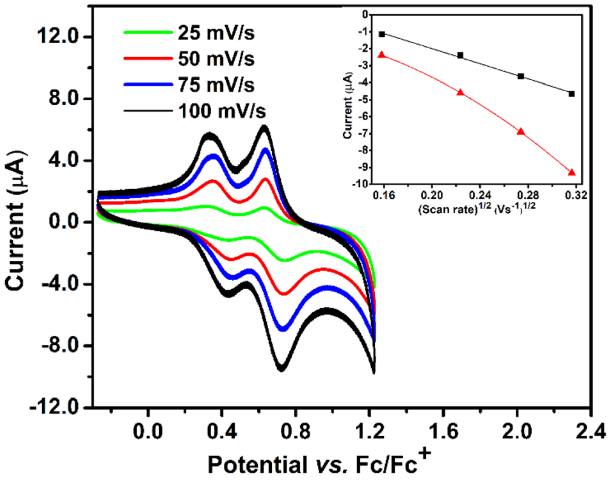

Fig. 3 Scan rate dependent cyclic voltammetry of **1** at scan rates from 25 mV s^{-1} to 100 mV s^{-1}. Inset: plots of current *vs.* (scan rate)$^{1/2}$ for the first oxidation wave (black) and second oxidation wave (red).

UV-vis optical properties

We examined the absorption properties of TPPB ligands and **1** (Fig. 4a). The TPPB ligand exhibited a broad band at 370 nm; it can be assigned to π to π* transitions of the aromatic moieties within the TPPB ligand. The solid-state diffuse reflectance absorption spectrum of **1** encompasses a broad range from 300 nm to 680 nm. Absorption of **1** is red-shifted compared to that of the TPPB ligand. The lone pair electrons from the nitrogen formed a conjugated bond with the neighboring benzene and pyridine ring, forming a π-extended conjugation system. The main absorption band of **1** is predominantly from the TPPB ligand. From the Tauc plot, the band gap of **1** was estimated at approximately 2 eV (Fig. 4b).

Theoretical calculations

To gain an in-depth insight into the electronic properties of compound **1** at the atomic level, we carried out quantum-mechanical first-principles density functional theory (DFT) calculations on its crystal structure. The fundamental electronic characteristics such as the band-gap, band structure, band-edge features, and density of states (DOS) of compound **1** are given in Fig. 5. As depicted in Fig. 5a, the electronic band structure displays a band-gap energy of 1.86 eV, indicating that **1** is a semiconductor with a moderate band gap. Furthermore, the band lines originating from the constituent atoms of **1** were obtained by analyzing the DOS. It reveals the conduction band minimum (CBM) and valence band minimum (VBM) generated by the electronic states of C and N, indicating that the organic linker, TPPB is critical to the electronic feature of **1** (Fig. 5b). Analysis of band-decomposed charge density provided a more detailed view of the VBM and CBM. We observed a high-degree of orbital overlap in the p orbitals of C and N. Specifically, the holes in the VBM are distributed over the benzene rings (Fig. 5c), whereas the electrons in the CBM pass through the C and N atoms of (4-(pyridin-4-yl)phenyl)amine (Fig. 5d). This implies the delocalization of π electrons in the VBM. Such a different appearance of the charge carriers at band edges means a spatial separation between electrons and holes, thereby preventing the fast recombination of charge carriers. The present theoretical results indicate that **1** is a semiconductor with a promising direct band-gap and spatial charge carrier separation.

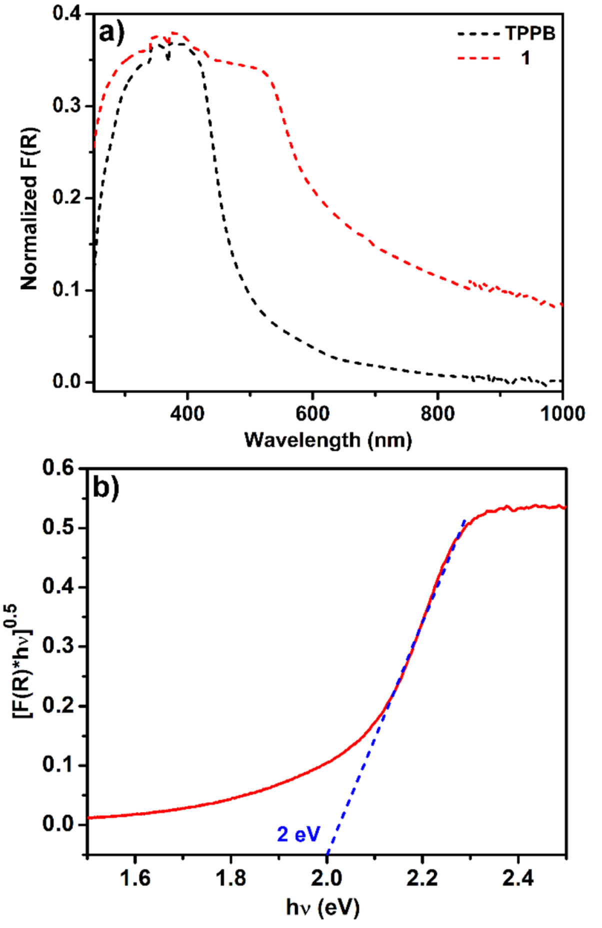

Fig. 4 (a) Diffuse reflectance UV-visible spectra of **1** and the TPPB ligand, and (b) Tauc plot to estimate the optical band gap.

Conductivity properties

After gathering sufficient experimental and theoretical structural information about **1**, we sought to investigate the electrical properties of **1**. The conductivity of **1** was measured using a two-probe single-crystal measurement. The conductivity measurements were conducted in three batches of crystals (Table S2†). Good quality crystals with a few micrometer sizes and no visible crack were selected and transferred onto the chip template. The two edges of the microcrystal using platinum as the contact metal were deposited by the focus-ion beam (FIB)[44,45] (inset, Fig. 6a). We obtained the conductivity value from 0.83 to 1.9 S cm^{-1} (Fig. 6a, S9a and b†). From the temperature-dependent experiments (Fig. 6b), it is observed that the incremental temperature increased electrical conductivity, indicating that **1** possesses semiconductive characteristics. The Arrhenius plot resulted in a linear relationship with an activation energy of 18 meV (Fig. 6c). The defects and charge hopping barriers may contribute to the discrepancy between the optical band gap (2 eV) and the experimental activation energy (18 meV).[12]

Photoconductivity

Photoconductivity is the process of the absorption of energy from light or the excitation of charge carriers from a lower energy state (HOMO) to a higher energy state (LUMO).[46] The charge carriers are free to mobilize until they return to the HOMO. An ordered and regular packing arrangement of **1** makes the movement of charge carriers feasible. From the density of states (DOS) analysis, an intermediate energy band gap of 1.86 eV was observed, which helps to promote the electron transfer from the valence band to the conduction band during excitation (Fig. 5a). The UV-visible diffuse reflectance spectrum (Fig. 4a) exhibited a broad absorption band near the visible region from 300 nm to 680 nm. Photoconductivity measurements were conducted to investigate the sensitivity of **1** towards light-induced current transport based on single crystals at potentials of 0 V to 1 V.

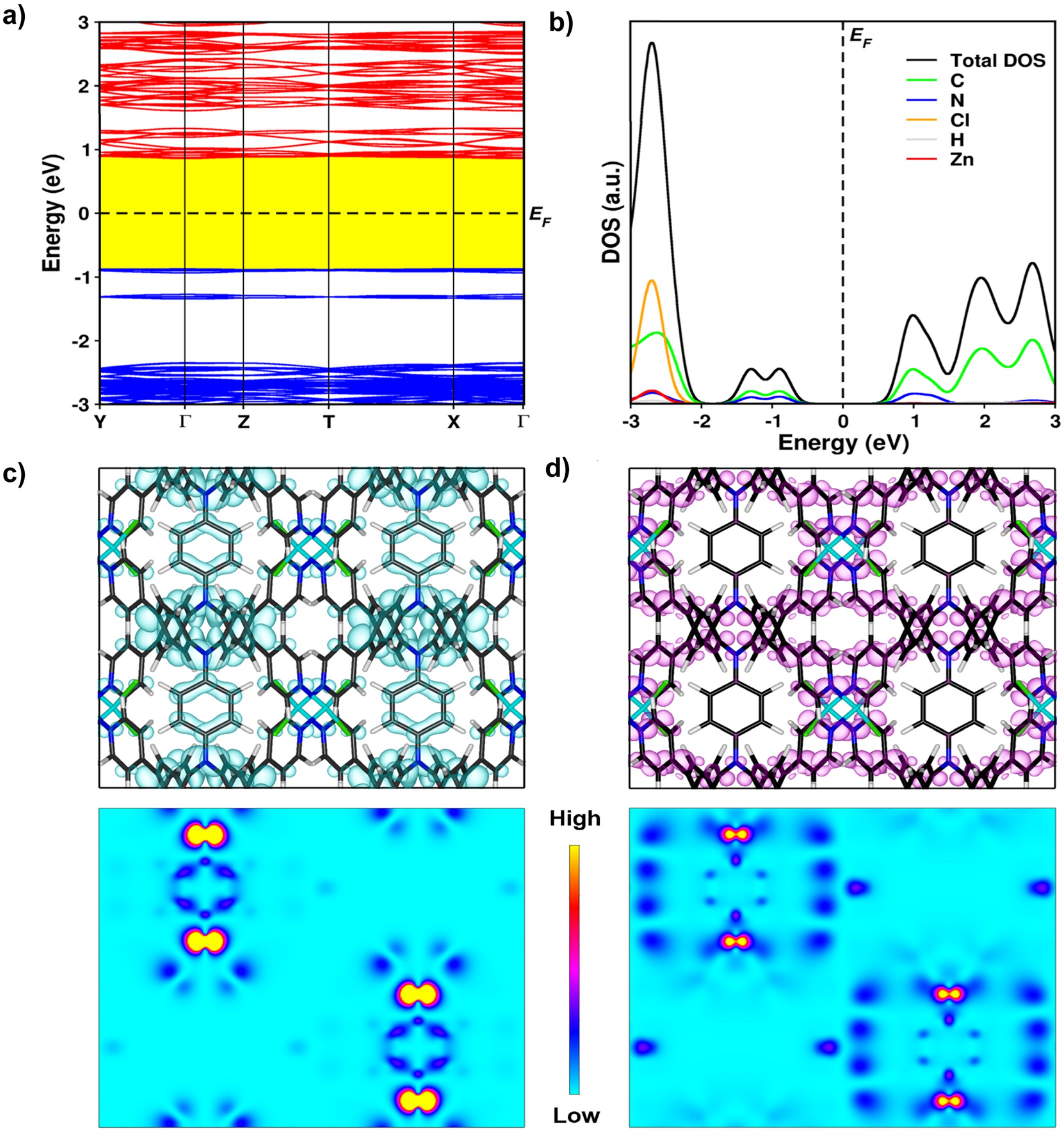

Fig. 5 (a) Calculated band structure and (b) density of states of **1**. Along the [100] crystallographic plane of **1**, the 3D iso-surface (upper panels) and 2D contour map (bottom panels) of the (c) valence band minimum (VBM) and (d) conduction band minimum (CBM), respectively.

The photocurrent responses were recorded in visible ranges, including 405 nm, 532 nm, and 633 nm (Fig. 7a) in optical power ranges of 2–50 mW. The photocurrents follow a linear relationship with light intensity. The optimal photoresponse was observed at $\lambda = 405$ nm with a photocurrent as high as 0.4 μA at 2000 W m^{-2} (Fig. 7b).

Responsivity and photoconductivity gain are two essential parameters in the discussion of photoconductivity. The term photoresponsivity indicates the photocurrent generated per unit of excitation power.[46] The value of photoresponsivity is obtained by multiplying the photoconductance by the square of the electrode spacing and dividing by the absorbed radiation power. The formula to calculate the responsivity value is $R = i_p/P$, where R is responsivity, P is the incident optical power on the effective area of a photoconductor, and i_p represents the photocurrent. An optimal responsivity was observed at 88 A W^{-1} with a wavelength of 405 nm and an optical intensity of 40 W m^{-2} (Fig. 7c).

One of the important criteria for photoconductivity is the photocarrier transport efficiency in a photoconductor. This can be determined using photoconductive gain (Γ) (detailed treatment in the ESI†). The gain value is the circulating number of charge carriers that pass through a photoconductor per unit of time before recombination.[46] It is convenient to think of the photoconductive gain in terms of the number of charge carriers that pass between the electrodes per second. The gain value at 269 A W^{-1} was obtained at $\lambda = 405$ nm and $I = 40$ W m^{-2} (Fig. 7d). It is noteworthy that the obtained value is higher

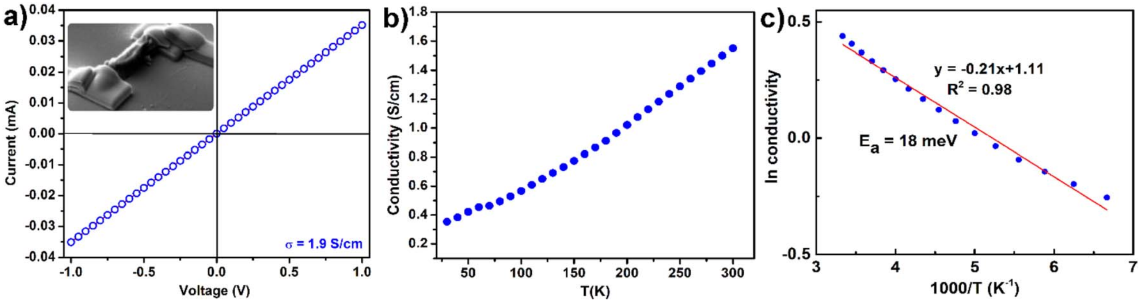

Fig. 6 (a) *I*–*V* curve for two-contact probe single crystal measurement, (b) electrical conductivity of **1** as a function of temperature, and (c) Arrhenius fitting of conductivity to temperature.

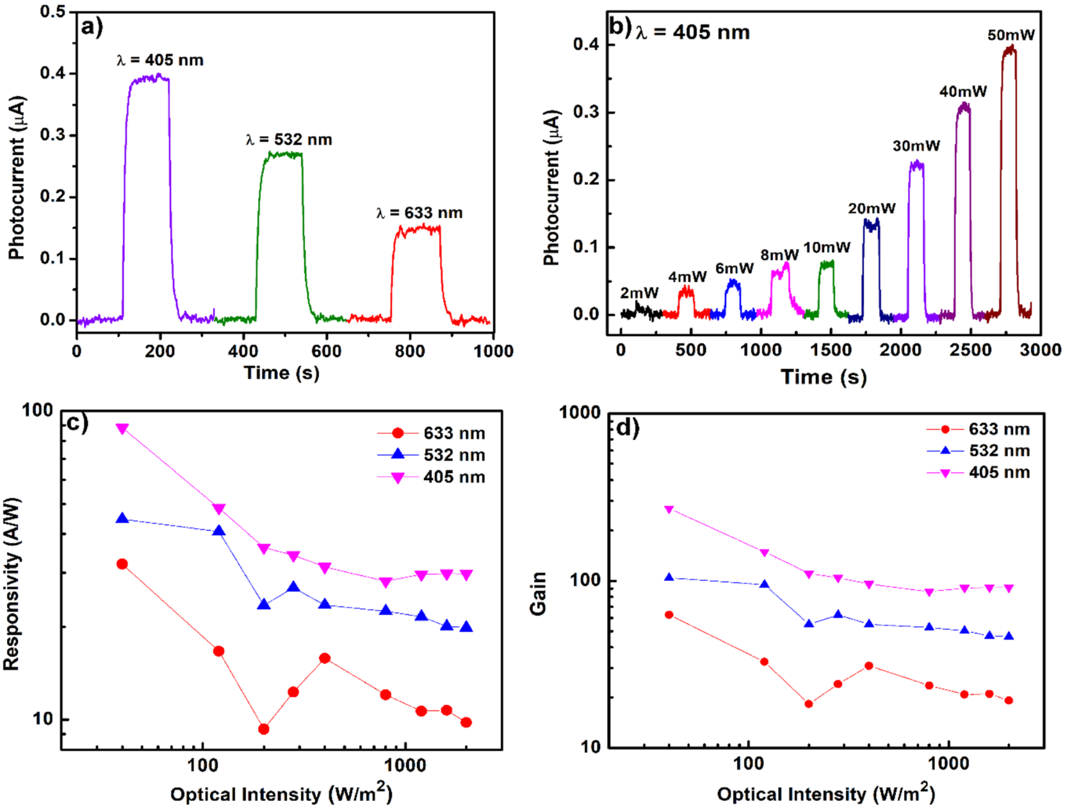

Fig. 7 (a) Photocurrent responses at excitation wavelengths of $\lambda = 405$, 532, and 633 nm, (b) a time-dependent photocurrent response at $\lambda = 405$ nm at different optical powers, (c) responsivity, and (d) photoconductive gain at the different excitation wavelengths.

compared to that of the well-known inorganic semiconductors (Table S3†) such as ZnS nanobelts (Γ ~0.5 A W^{-1}),[47] ZnO nanospheres (Γ ~5 A W^{-1}),[48] and Nb$_2$O$_5$ nanobelts (Γ ~6 A W^{-1}).[49]

The carrier lifetime was measured using time-resolved photoconductivity. Lifetime is one of the critical parameters for determining photocarrier transport efficiency, as the time-excited electrons stay in the LUMO before being terminated by recombination. As defined by the different charge distributions (Fig. 5c and d) of the TPPB linkers, spatial separation between electrons and holes prevents the fast recombination of charge carriers. The calculations are in good agreement with the lifetime experiments. We obtained the carrier lifetime (τ) values by curve fitting using the time-dependent stretched exponential function (detailed treatment in the ESI†). The lifetime value was 8.8 s at $\lambda = 405$ nm (Fig. 8a). For 532 nm and 633 nm (Fig. S11b and d†), the lifetime value is 8.6 s and 6.6 s, respectively. The lifetime of **1** is several orders of magnitude longer than that of conventional inorganic semiconductors such as silicon (τ = 1–10 μs)[50] and GaAs (τ < 1 ns).[51] For semiconductor nanomaterials which exhibited a similar electron–hole spatial separation like **1**, a relatively long lifetime was obtained, such as ZnO nanofilms (τ = 8–100 s),[52] TiO$_2$ nanorods (τ = 0.1–100 s),[53] GaN nanowires (τ > 10 s),[54] InSe nanosheets (τ = 10–500 s),[55] and MoSe$_2$ nanosheets (τ = 5–20 s).[56] Carrier lifetime achieved stabilization at a higher optical

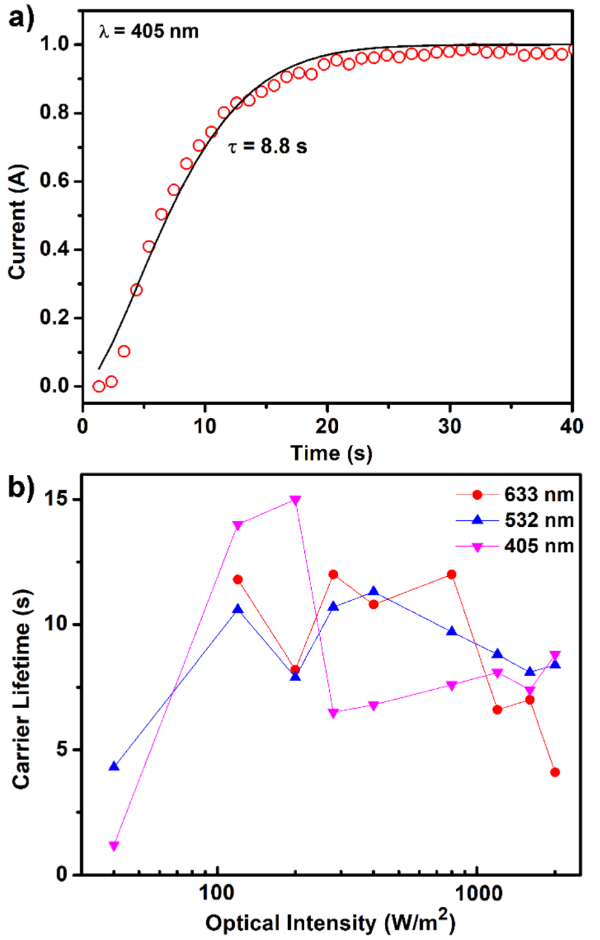

Fig. 8 (a) Fitting curve of the lifetime at $\lambda = 405$ nm with an intensity of 2000 W m^{-2} and (b) carrier lifetime at different excitation wavelengths.

intensity, as illustrated in Fig. 8b. Owing to its ultra-long carrier lifetime, **1** is of great interest as a promising photocatalyst.

Conclusions

This paper demonstrates that a semiconductive 2D coordination framework could be achieved by incorporating a triphenylamine derivative as a linker. Synthesis of the TPPB linker using Suzuki coupling is a straightforward method with a high yield (>80%). A redox-active TPPB linker promotes a π-conjugated pathway coupled with a densely interpenetrated network. Experimental studies and electronic band structure analysis confirmed the semiconductor behavior of **1**. A moderate band gap and photoconductivity are correlated, as we observed a linear relationship in the occurrence of photocurrent when optical power increased. The broad absorption spectrum in the visible region indicates that the value of photocurrent is in the range of 0.4 μA. A long carrier lifetime was observed in **1**; the fitting time is 8.8 s before the charge recombination. **1** possesses a long carrier lifetime, this property may be of further interest as a potential candidate for photocatalysis. We anticipate that our approach of using a bis(triarylamine) ligand will open up new avenues for in-depth investigation in semiconductive coordination polymers through further innovation and manipulation of different ligands.

Data availability

ESI† is available, which contains the details methods and synthesis of materials, physical characterization, conductivity and photoconductivity measurements, single crystal X-ray data, and computational details. This article's crystallographic information for the structure has been deposited at the Cambridge Crystallographic Data Centre under deposition number 2173865.

Author contributions

C. M. N., R. S. C., and M. K. L. conceived the project, designed the experiments, and wrote the manuscript. C. M. N. performed the synthesis and experiments. K. F. H. and K. Y. L. measured the conductivity and photocurrent. B. S., E. B., and M. H. contributed to the theoretical studies.

Conflicts of interest

The authors declare no conflict of interest.

Acknowledgements

The authors acknowledge the mass spectrometry technical research services from NTU Consortia of Key Technologies and scanning electron microscopy (SEM) measurements from Mei-Ying Chung. We acknowledge Yuh-Sheng Wen for assisting in solving the single crystal structure. C. M. N is grateful for the postdoctoral fellowship supported by the Ministry of Science and Technology, Taiwan, under grant numbers 110-2113-M-002-009 and 110-2811-M-002-556. B. S., E. B., and M. H. thank the Center of Atomic Initiative for New Materials (project no. 112L4000, 110L9008, 111-2123-M-002-009 and 111-2113-M-002-003) for the funding support. We thank the Computer and Information Networking Center, National Taiwan University, for providing high-performance computing facilities.

Notes and references

1 A. J. Clough, N. M. Orchanian, J. M. Skelton, A. J. Neer, S. A. Howard, C. A. Downes, L. F. J. Piper, A. Walsh, B. C. Melot and S. C. Marinescu, *J. Am. Chem. Soc.*, 2019, **141**, 16323–16330.
2 H. Banda, J.-H. Dou, T. Chen, N. J. Libretto, M. Chaudhary, G. M. Bernard, J. T. Miller, V. K. Michaelis and M. Dincă, *J. Am. Chem. Soc.*, 2021, **143**, 2285–2292.
3 X. Huang, P. Sheng, Z. Tu, F. Zhang, J. Wang, H. Geng, Y. Zou, C.-a. Di, Y. Yi, Y. Sun, W. Xu and D. Zhu, *Nat. Commun.*, 2015, **6**, 7408.
4 C. W. Zengqiang Gao, J. Li, Y. Zhu, Z. Zhang and W. Hu, *Acta Biochim. Biophys. Sin.*, 2021, **37**, 2010025.
5 P. Amo-Ochoa, L. Welte, R. González-Prieto, P. J. Sanz Miguel, C. J. Gómez-García, E. Mateo-Martí, S. Delgado,

J. Gómez-Herrero and F. Zamora, *Chem. Commun.*, 2010, **46**, 3262–3264.

6 S. Henfling, A. Kultaeva, A. Pöppl, J. Klose, B. Kersting, K. V. Domasevitch and H. Krautscheid, *Inorg. Chem.*, 2021, **60**, 9008–9018.

7 A. Chandra, D. Das, J.-O. Castro, K. Naskar, S. Jana, A. Frontera, P. Pratim Ray and C. Sinha, *Inorg. Chim. Acta*, 2021, **518**, 120253.

8 N. Lahiri, N. Lotfizadeh, R. Tsuchikawa, V. V. Deshpande and J. Louie, *J. Am. Chem. Soc.*, 2017, **139**, 19–22.

9 X. Huang, H. Li, Z. Tu, L. Liu, X. Wu, J. Chen, Y. Liang, Y. Zou, Y. Yi, J. Sun, W. Xu and D. Zhu, *J. Am. Chem. Soc.*, 2018, **140**, 15153–15156.

10 H. Qi, B. Liang and U. Kaiser, *SmartMat*, 2021, **2**, 131–138.

11 J. Ouyang, *SmartMat*, 2021, **2**, 263–285.

12 Z. Meng, C. G. Jones, S. Farid, I. U. Khan, H. M. Nelson and K. A. Mirica, *Angew. Chem., Int. Ed.*, 2022, **61**, e202113569.

13 L. S. Xie, G. Skorupskii and M. Dincă, *Chem. Rev.*, 2020, **120**, 8536–8580.

14 J.-H. Dou, M. Q. Arguilla, Y. Luo, J. Li, W. Zhang, L. Sun, J. L. Mancuso, L. Yang, T. Chen, L. R. Parent, G. Skorupskii, N. J. Libretto, C. Sun, M. C. Yang, P. V. Dip, E. J. Brignole, J. T. Miller, J. Kong, C. H. Hendon, J. Sun and M. Dincă, *Nat. Mater.*, 2021, **20**, 222–228.

15 Y. Kobayashi, B. Jacobs, M. D. Allendorf and J. R. Long, *Chem. Mater.*, 2010, **22**, 4120–4122.

16 J. Cui and Z. Xu, *Chem. Commun.*, 2014, **50**, 3986–3988.

17 T. Kambe, R. Sakamoto, T. Kusamoto, T. Pal, N. Fukui, K. Hoshiko, T. Shimojima, Z. Wang, T. Hirahara, K. Ishizaka, S. Hasegawa, F. Liu and H. Nishihara, *J. Am. Chem. Soc.*, 2014, **136**, 14357–14360.

18 X. Sun, K.-H. Wu, R. Sakamoto, T. Kusamoto, H. Maeda, X. Ni, W. Jiang, F. Liu, S. Sasaki, H. Masunaga and H. Nishihara, *Chem. Sci.*, 2017, **8**, 8078–8085.

19 R. Dong, P. Han, H. Arora, M. Ballabio, M. Karakus, Z. Zhang, C. Shekhar, P. Adler, P. S. Petkov, A. Erbe, S. C. B. Mannsfeld, C. Felser, T. Heine, M. Bonn, X. Feng and E. Cánovas, *Nat. Mater.*, 2018, **17**, 1027–1032.

20 X. Huang, S. Zhang, L. Liu, L. Yu, G. Chen, W. Xu and D. Zhu, *Angew. Chem., Int. Ed.*, 2018, **57**, 146–150.

21 T. Pal, S. Doi, H. Maeda, K. Wada, C. M. Tan, N. Fukui, R. Sakamoto, S. Tsuneyuki, S. Sasaki and H. Nishihara, *Chem. Sci.*, 2019, **10**, 5218–5225.

22 M. Hmadeh, Z. Lu, Z. Liu, F. Gándara, H. Furukawa, S. Wan, V. Augustyn, R. Chang, L. Liao, F. Zhou, E. Perre, V. Ozolins, K. Suenaga, X. Duan, B. Dunn, Y. Yamamto, O. Terasaki and O. M. Yaghi, *Chem. Mater.*, 2012, **24**, 3511–3513.

23 M. G. Campbell, S. F. Liu, T. M. Swager and M. Dincă, *J. Am. Chem. Soc.*, 2015, **137**, 13780–13783.

24 L. E. Darago, M. L. Aubrey, C. J. Yu, M. I. Gonzalez and J. R. Long, *J. Am. Chem. Soc.*, 2015, **137**, 15703–15711.

25 M.-S. Yao, X.-J. Lv, Z.-H. Fu, W.-H. Li, W.-H. Deng, G.-D. Wu and G. Xu, *Angew. Chem., Int. Ed.*, 2017, **56**, 16510–16514.

26 M. E. Ziebel, L. E. Darago and J. R. Long, *J. Am. Chem. Soc.*, 2018, **140**, 3040–3051.

27 J. Park, A. C. Hinckley, Z. Huang, D. Feng, A. A. Yakovenko, M. Lee, S. Chen, X. Zou and Z. Bao, *J. Am. Chem. Soc.*, 2018, **140**, 14533–14537.

28 B. Hoppe, K. D. J. Hindricks, D. P. Warwas, H. A. Schulze, A. Mohmeyer, T. J. Pinkvos, S. Zailskas, M. R. Krey, C. Belke, S. König, M. Fröba, R. J. Haug and P. Behrens, *CrystEngComm*, 2018, **20**, 6458–6471.

29 V. Rubio-Giménez, M. Galbiati, J. Castells-Gil, N. Almora-Barrios, J. Navarro-Sánchez, G. Escorcia-Ariza, M. Mattera, T. Arnold, J. Rawle, S. Tatay, E. Coronado and C. Martí-Gastaldo, *Adv. Mater.*, 2018, **30**, 1704291.

30 J. Park, M. Lee, D. Feng, Z. Huang, A. C. Hinckley, A. Yakovenko, X. Zou, Y. Cui and Z. Bao, *J. Am. Chem. Soc.*, 2018, **140**, 10315–10323.

31 L. Qu, H. Iguchi, S. Takaishi, F. Habib, C. F. Leong, D. M. D'Alessandro, T. Yoshida, H. Abe, E. Nishibori and M. Yamashita, *J. Am. Chem. Soc.*, 2019, **141**, 6802–6806.

32 B. E. Koene, D. E. Loy and M. E. Thompson, *Chem. Mater.*, 1998, **10**, 2235–2250.

33 P. Strohriegl and J. V. Grazulevicius, *Adv. Mater.*, 2002, **14**, 1439–1452.

34 J.-Q. Li, S.-W. Ke, T. Yan, Y.-Y. Li, Y. Zhou, M. Kurmoo, J. Su and J.-L. Zuo, *Inorg. Chem.*, 2021, **60**, 8331–8338.

35 G. C. Solomon, D. Q. Andrews, R. P. Van Duyne and M. A. Ratner, *ChemPhysChem*, 2009, **10**, 257–264.

36 J. Schäfer, M. Holzapfel, B. Mladenova, D. Kattnig, I. Krummenacher, H. Braunschweig, G. Grampp and C. Lambert, *J. Am. Chem. Soc.*, 2017, **139**, 6200–6209.

37 S. Amthor, B. Noller and C. Lambert, *Chem. Phys.*, 2005, **316**, 141–152.

38 D. C. Mayer, A. Manzi, R. Medishetty, B. Winkler, C. Schneider, G. Kieslich, A. Pöthig, J. Feldmann and R. A. Fischer, *J. Am. Chem. Soc.*, 2019, **141**, 11594–11602.

39 A. Spek, *Acta Crystallograpr., Sect. C*, 2015, **71**, 9–18.

40 S. R. Ahrenholtz, C. C. Epley and A. J. Morris, *J. Am. Chem. Soc.*, 2014, **136**, 2464–2472.

41 S. Patwardhan and G. C. Schatz, *J. Phys. Chem. C*, 2015, **119**, 24238–24247.

42 B. A. Johnson, A. Bhunia, H. Fei, S. M. Cohen and S. Ott, *J. Am. Chem. Soc.*, 2018, **140**, 2985–2994.

43 A. J. Bard and L. R. Faulkner, *Electrochemical Methods: Fundamentals and Applications*, John Wiley & Sons, Inc., New York, 2nd edn, 2001.

44 A. Pathak, J.-W. Shen, M. Usman, L.-F. Wei, S. Mendiratta, Y.-S. Chang, B. Sainbileg, C.-M. Ngue, R.-S. Chen, M. Hayashi, T.-T. Luo, F.-R. Chen, K.-H. Chen, T.-W. Tseng, L.-C. Chen and K.-L. Lu, *Nat. Commun.*, 2019, **10**, 1721.

45 A. I. Inamdar, B. Sainbileg, C.-J. Lin, M. Usman, S. Kamal, K.-R. Chiou, A. Pathak, T.-T. Luo, K. S. Bayikadi, R. Sankar, J.-W. Chen, T.-W. Tseng, R.-S. Chen, M. Hayashi, M.-H. Chiang and K.-L. Lu, *ACS Appl. Mater. Interfaces*, 2022, **14**, 12423–12433.

46 R. H. Bube, *Photoconductivity of Solids*, John Wiley & Sons, Inc., New York, 1960.

47 X. Fang, Y. Bando, M. Liao, U. K. Gautam, C. Zhi, B. Dierre, B. Liu, T. Zhai, T. Sekiguchi, Y. Koide and D. Golberg, *Adv. Mater.*, 2009, **21**, 2034–2039.

48 M. Chen, L. Hu, J. Xu, M. Liao, L. Wu and X. Fang, *Small*, 2011, **7**, 2449–2453.

49 X. Fang, L. Hu, K. Huo, B. Gao, L. Zhao, M. Liao, P. K. Chu, Y. Bando and D. Golberg, *Adv. Funct. Mater.*, 2011, **21**, 3907–3915.

50 P. Rosenits, T. Roth, W. Warta, S. Reber and S. W. Glunz, *J. Appl. Phys.*, 2009, **105**, 053714.

51 X. Zou, C. Li, X. Su, Y. Liu, D. Finkelstein-Shapiro, W. Zhang and A. Yartsev, *ACS Appl. Mater. Interfaces*, 2020, **12**, 28360–28367.

52 C. H. Lin, R. S. Chen, Y. K. Lin, S. B. Wang, L. C. Chen, K. H. Chen, M. C. Wen, M. M. C. Chou and L. Chang, *Appl. Phys. Lett.*, 2017, **110**, 052101.

53 R.-S. Chen, Y.-L. Liu, C.-H. Chan and Y.-S. Huang, *Appl. Phys. Lett.*, 2014, **105**, 153107.

54 R. S. Chen, C. Y. Lu, K. H. Chen and L. C. Chen, *Appl. Phys. Lett.*, 2009, **95**, 233119.

55 H.-W. Yang, H.-F. Hsieh, R.-S. Chen, C.-H. Ho, K.-Y. Lee and L.-C. Chao, *ACS Appl. Mater. Interfaces*, 2018, **10**, 5740–5749.

56 M. Anandan, Y.-S. Chang, C.-Y. Chen, C.-J. Ho, C.-M. Cheng, H.-R. Chen, T.-Y. Fu, Y.-W. Chu, K.-Y. Lee, L.-C. Chao and R.-S. Chen, *Phys. E*, 2022, **135**, 114988.